Geomech. Geophys. Geo-energ. Geo-resour. (2024) 10:149
https://doi.org/10.1007/s40948-024-00844-z

RESEARCH

Remote sensing and aeromagnetic mapping for unveiling mineralization potential: Nuqrah Area, Saudi Arabia

Saad S. Alarifi · Reda Abdu Yousef El-Qassas · Ali Elsayed Ali Omar · Ahmad M. Al-Saleh · Peter András · Ahmed M. Eldosouky

Received: 26 April 2024 / Accepted: 18 July 2024
© The Author(s) 2024

Abstract Lately, Saudi Arabia has been developing its mineral exploration. However, comprehensive studies of the collected data are not accessible. Thus, the purpose of this research is to identify and map the hydrothermal alteration zones and structural lineaments that regulate the mineral occurrences in the Nuqrah region of the Kingdom of Saudi Arabia using remote sensing and aeromagnetic data. To achieve the desired goal of the study, ASTER remote sensing data were employed, and they were processed in several ways, including principal component analysis, band ratio, and false color composites to reveal the zones of alteration and structure lineaments. In addition, aeromagnetic data was employed to map the lineaments controlling the mineralization. These datasets were integrated using GIS tools to generate a new mineralization potential map of the Nuqrah area, which was classified into three classes: low, moderate, and high probability mineralization. The results showed thirteen intriguing anomalies (high potential mineralization) dispersed over the research area to be prospected. Additionally, techniques such as residual, regional, first vertical derivative, and tilt derivative were utilized to detect the potential mineral-related geologic structures. The results were validated by plotting known mineralization sites on our maps. Six significant faulting trends have been found, according to the lineament map and rose diagrams from remote sensing: NE–SW, WNW–ESE, N–S, ENE–WSW, NNE–SSW, NW–SE, and E–W. The research region is most affected by the NW–SE, ENE–WSW, E–W, and N–S trends, which are organized in decreasing order of magnitude, according to the rose diagram of the aeromagnetic maps. The applied approach can be employed to map potential mineral deposits in Saudi Arabia and similar zones around the globe.

S. S. Alarifi (✉) · A. M. Al-Saleh
Department of Geology and Geophysics, College of Science, King Saud University, P.O. Box 2455, 11451 Riyadh, Saudi Arabia
e-mail: ssalarifi@ksu.edu.sa

R. A. Y. El-Qassas
Ground Geophysics Department, Exploration Division, Nuclear Materials Authority (NMA), P.O. Box 530, Maadi, Cairo, Egypt

A. E. A. Omar
Sedimentary Radioactive Deposits Department, Research Division, Nuclear Materials Authority (NMA), P.O. Box: 530, Maadi, Cairo, Egypt

P. András
Faculty of Natural Sciences, Matej Bel University in Banska Bystrica, Tajovského 40, 974 01 Banská Bystrica, Slovakia

A. M. Eldosouky (✉)
Department of Geology, Faculty of Science, Suez University, Suez 43221, Egypt
e-mail: dr_a.eldosoky@yahoo.com

Published online: 03 September 2024

Content courtesy of Springer Nature, terms of use apply. Rights reserved.

Article Highlights

- Generate new maps for mineral potentialty in Nuqrah area, Saudi Arabia.
- Aeromagnetic and RS data were used to achieve the aim of the study.
- These maps were used to find potential mineral-related geologic structures.
- Indicated six major faulting trends controlling the area.

Keywords Mineralization potentiality · Remote sensing · Alteration zones · Aeromagnetic · Structures · Saudi Arabia

1 Introduction

Recently, geospatial technologies have helped increase our knowledge of the earth and its treasures. This is done by providing a way to gather data very quickly and convert it into important information. Remote sensing (RS) and geographic information system (GIS) technology have proven their usefulness and role as tools that can be applied confidently and efficiently in all disciplines of earth sciences, especially in geological mapping, mineral exploration, flash flood hazards, seismotectonic hazards, and urbanization through the capabilities of processing satellite images (Hajibapir et al. 2014; Arnous and Omar 2018; Arnous et al. 2018; Omar 2021; Saad et al. 2020; Eldosouky et al. 2021; Omar et al. 2021; Bencharef et al. 2022; Hegab et al. 2022; Kharbish et al. 2022; Mahdi et al. 2022; El-Qassas et al. 2023; Omar et al. 2021, 2023a, b). In this study, the spaceborne Advanced Thermal Emission and Reflection Radiometer (ASTER) image data were used to identify the hydrothermal alteration mineral (HAM) areas associated with mineralization areas. The HAM has spectral absorption properties in the near infrared (VNIR) and short-wave infrared (SWIR) regions (Abrams et al. 1983).

The Magnetic data in geophysical exploration is a powerful method for locating subsurface structures, magnetic objects and mineral exploration (Eldosouky et al. 2022a). This method uses the Earth's natural magnetic field to detect anomalies that may be investigated and studied further. It deals with the variations in magnetization between various rock types to help identify zones of interest. The magnetic method was developed over time with improved accuracy and resolution. It can map out the subsurface structures, such as faults, shear zones, and contacts which may form pathways of mineralization or ore deposits and mineral exploration (Assran et al. 2019; Eldosouky et al. 2021, 2022b; Pham et al., 2021; Elkhateeb et al. 2021; El-Qassas et al. 2021, 2023; Abdelrahman et al. 2023; Ekwok et al. 2023, 2024).

The Arabian–Nubian shield is made up mostly of juvenile crust that developed during Cryogenian-Ediacaran time through the amalgamation of several oceanic terranes. These terranes are underlain by metamorphosed volcano-sedimentary belts that are favorable hosts for volcanogenic massive sulphide deposits. These mineral occurrences are often clustered in metallogenic belts and provinces, and one of the most prominent of these is the Nuqrah belt in the north Central Arabian shield. Mineral occurrences in this belt have been worked since ancient times (the third or second millenium B.C.) with the last known excavations taking place in the A.D. 675–835 period (Heck 1999), especially at Nuqra South which is one of the largest historic copper mines in the Arabian Shield (Morony 2019).

In our study, we aim to produce new mineral potentiality maps for Nuqrah area from integration of Aster and aeromagnetic data. To achieve this goal, we applied different aeromagnetic data processing approaches, band ratio (BR), principal component analysis (PCA), and false color composites (FCC) methodologies. The visionary aspect of our study is the extended integration of ASTER with aeromagnetic data employing GIS tools. This approach allows for accurate and detailed mapping of mineralized zones and structural lineaments, which has not been considerably accomplished in the Nuqrah territory, Saudi Arabia, an area with limited previous investigations. The results will be employed to map the promising altered zones and dominant structures. This will lead to excessive and detailed ground studies for exploitation purposes.

Content courtesy of Springer Nature, terms of use apply. Rights reserved.

2 Geology

It is now well established that the Arabian Shield is made up of several tectonostratigraphic terranes that amalgamated in the period 605–780 Ma, following the clousure of the Mozambique Ocean and the ensuing collision between east and west Gondwana (Johnson et al. 2011). The Nuqrah region lies within the northern extremity of the Afif composite terrane (Fig. 1), and as the name indicates this terrane is made up of a number of volcanomagmatic arcs and subterranes. The volcanic arc in the Nuqrah area is distinctly older than others further south, and the initial 143Nd/144Nd ratios are in the range +1.6 to +6.9 (Duyverman et al 1982) signifying a juvenile upper mantle source with little or no older crustal component. The best age estimate for this part of the shield is 839 ± 23 Ma based on a U–Pb concordant age from zircons separated from a rhyolite collected near the Nuqrah mines (Calvez et al 1983).

The Nuqrah region (Fig. 1) is underlain by mafic and subordinate acidic volcanics and sediments that underwent greenschist grade metamorphism; this assemblage was assigned to the Hulayfah Group by Delfour (1977). The name Isamah Formation was later proposed by Johnson (2005) to replace the terms "Hulayfah group" for sedimentary and volcanic rocks east of the Hulayfah suture zone, which he believes

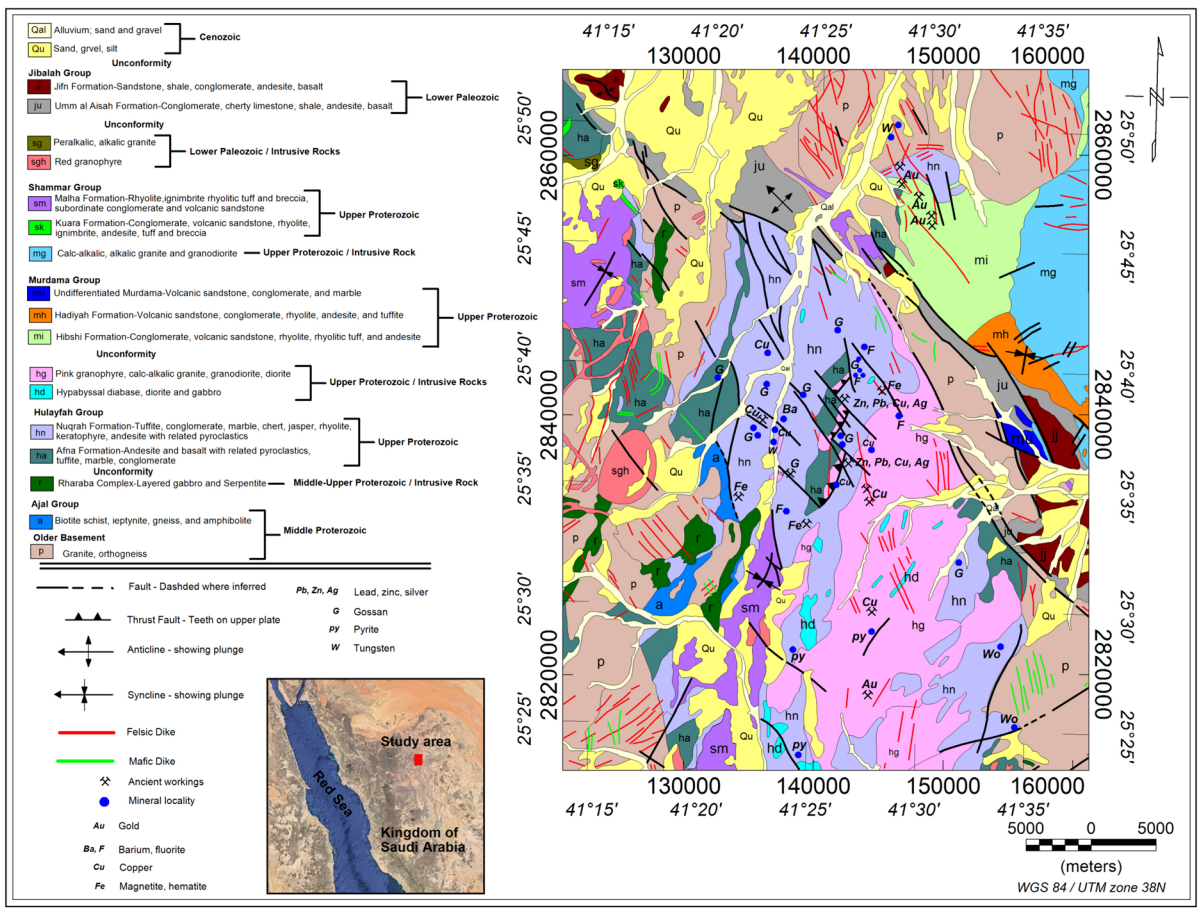

Fig. 1 Geologic map of Nuqrah area (Kingdom of Saudi Arabia Ministry of Petroleum and Mineral Resources 1977), Kingdom of Saudi Arabia, with a location map (inset)

Content courtesy of Springer Nature, terms of use apply. Rights reserved.

to be older than other belts assigned to the Hulayfah Group. According to Delfour (1977) rocks of the Hulayfah Group are exposed in steeply folded, nonh-trending belts that are offset by the sinistral strike-slip faults of the Najd system.

On the basis of their stratigraphy, rock successions within these belts can be divided into the Afna and Nuqrah formations (Fig. 1). The older Afna formation consists mostly of basic volcanics, while the younger Nuqrah formation has a bi-modal mafic-felsic nature. The Afna formation has a thickness of nearly 2000 m, and it lies unconformably upon the basalts of the Bi'r Tuluhah Ophiolitic Complex; at this locality the contact is marked by a basal conglomerate which grades upward to alternating beds of calcareous and dolomitic marble, that may reach a thickness of 300 m at the type locality in Jabal Afinah. Above these marbles is a 300 m thick rhyolitic tuff member. Northwards, this member is replaced by pyroclastics that eventually grade to red siltstone. The upper Nuqrah subunit has an average thickness of 4000 m, most of which is made up of andesitic or basaltic lava flows, with intercalated tuff, breccia, agglomerate, marble and green siltstone. Within the belt containing the Nuqrah gossans and ancient workings, marble lenses alternate with graphitic tuff and sulfide mineralization (Delfour 1977).

3 Data used and methods

3.1 Remote sensing (RS)

The study area is covered by one ASTER level L1T 00302072004080000 scene that was acquired on 7-2-2004, with different spatial resolutions for the multispectral and panchromatic bands (Aita and Omar 2021; El-Qassas et al. 2023). It has the qualities of high spatial and spectral resolution in addition to being corrected radiometrically, atmospherically (Flaash), and geometrically in the UTM projection WSG84 zone 37N. False colour composites (FCC), band ratios (BR), and principal component analysis (PCA) are just a few of the techniques used on ASTER satellite data to identify the various HAM related to the mineralization in the studied area. ENVI 5.3 and Arc GIS 10.5 were used to manipulate, preprocess, and process this data. The Eq. (1) was used to apply the thresholding process on PCA and BR approaches to eliminate the various HAM from low concentration values as well as to extract and delineate halo zones of these minerals.

$$\text{Mean} + n * (\text{Standard Deviation}) \quad (1)$$

where n is 1 or 2, or 3.

Spectral properties of HAMs in ASTER data:

According to laboratory spectral characteristics from the USGS Mineral Spectral Library (Clark et al. 1993), which is imported from the ENVI version 5.3 software, the Fe-oxide/hydroxide, phyllic, argillic, and propylitic alteration types were identified and characterized in the VNIR-SWIR range (Fig. 2a, b) using the following: (1) Sericite (propylitic alteration) has a strong absorption feature at 2.20 µm (6th ASTER band), resulting from AL–O–H absorption, as well as a less strong absorption feature at 2.33 µm (8th ASTER band, resulting from Fe-, Mg–O–H absorption); (2) The argillic-altered rocks (kaolinite and alunite), which display AL–O–H absorption properties at 2.20 and 2.17 µm (5th ASTER band), respectively (Rowan et al. 2003); (3) Propylitic-altered rocks (chlorite, epidote, and carbonates, most notably calcite), which display an absorption feature at 2.33 µm (8th ASTER band) owing to vibrational interactions between Fe–O–H, Mg–O–H, and CO_3 (Rowan and Mars 2003; Tommaso and Rubinstein 2007); (4) Hematite, goethite, and limonite all display notable Fe^{3+} absorption features at 0.9–70.83 and 0.48 µm, respectively, (1st, and 3rd ASTER bands) according to (Hunt 1977). Jarosite shows Fe–O–H absorption characteristics at 0.94 and 2.27 µm (ASTER Band 7) (Fig. 2b).

3.2 Aeromagnetic

The study area was included in aeromagnetic survey between 1965 and 1966 for the Ministry of Petroleum and Mineral Resources of the Kingdom of Saudi Arabia. This survey was achieved by a Consortium of Aero Service Corporation, Hunting Geology and

Content courtesy of Springer Nature, terms of use apply. Rights reserved.

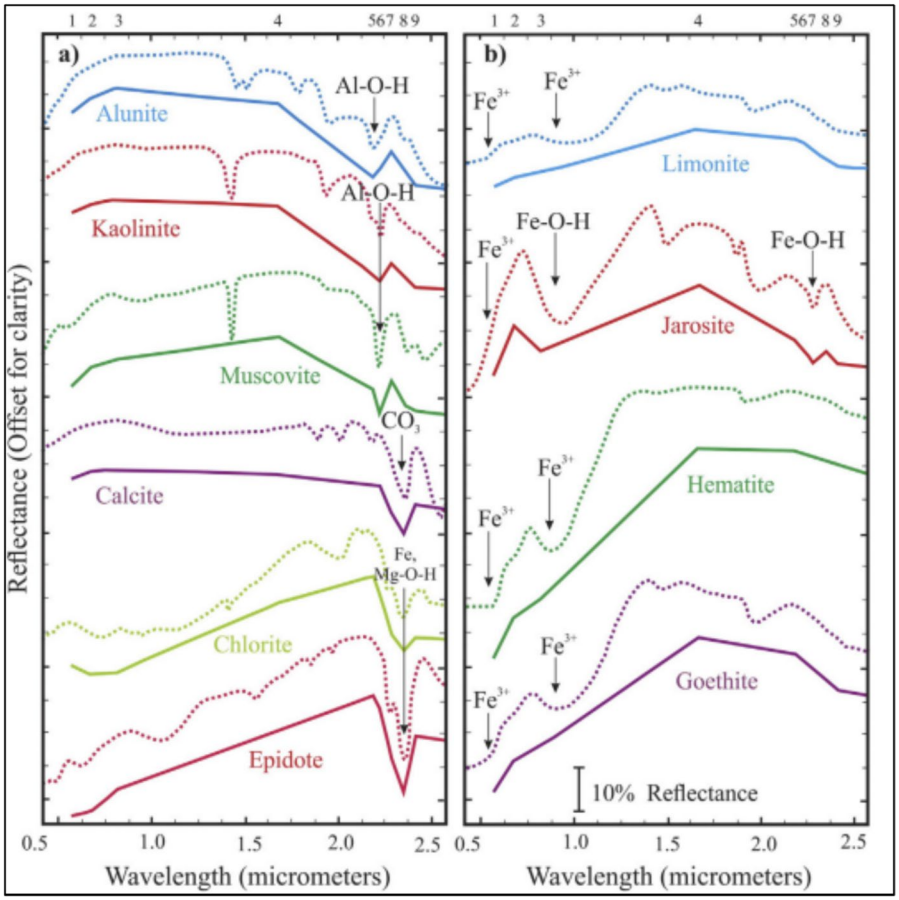

Fig. 2 Laboratory spectra of common hydrothermal alteration minerals showing (**a**) the laboratory spectra that are used in this study are grouped according to alteration assemblages and include muscovite, which is associated with phyllic alteration; kaolinite and alunite are associated with argillic alteration; epidote, chlorite, and calcite are associated with propylitic alteration; and (**b**) the laboratory spectra of limonite, jarosite, hematite, and goethite

Geophysics Limited, and Lockwood Survey Corporation Limited, under the supervision of the Bureau de Recherches Géologiques et Minières. The Fluxgate Gulf Mark III magnetometer with analog recording was used to conduct this survey. The flight lines for the aeromagnetic survey were flown along parallel traverse lines oriented in a NE-SW direction, with an azimuth of 45° from the true north and 800 m spacing (Aero Service 1966). The tie lines were flown 150° away from true north at an azimuth of NW–SE, at a right angle to the direction of the flight line. The tie lines were spaced at intervals of 16 km. Total magnetic intensity (TMI) measurements were made at a sensor altitude of 150 m above the ground (Aero Service 1966).

The reduced to the pole (RTP) grid map was utilized to identify the magnetic source bodies. Fast Fourier transformation (FFT) was used in the ongoing study to create the radially averaged power spectrum, residual, and regional magnetic component maps from the RTP aeromagnetic data. The first vertical derivative (FVD), and tilt derivative (TDR) were applied to the RTP airborne magnetic data. These maps were used to find potential mineral-related geologic structures (faults, contacts, shear zones, etc…). Where, they offer boundaries of sources at shallow and deep depths.

Gunn (1975) provides the formula for the vertical derivative as follows:

$$M_z(x,y) = M(x,y)\sqrt{\left(\frac{x^2+y^2}{n}\right)^n} \quad (2)$$

Content courtesy of Springer Nature, terms of use apply. Rights reserved.

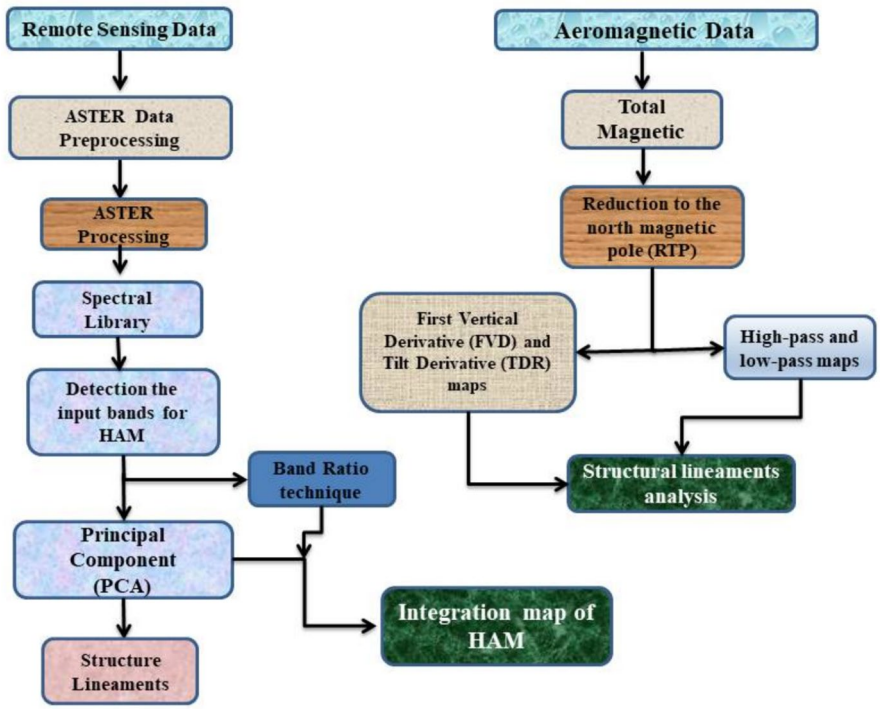

Fig. 3 Flow chart showing the remote sensing and aeromagnetic data

where M_z (x, y) is the vertical derivative of the magnetic field. M (x, y) refer to the original magnetic field. x *and* y represent the spatial coordinates. n is the order of the derivative.

This equation can be rewritten to be as:

$$M_z(x, y) = M(x, y)\left(\frac{x^2 + y^2}{n}\right)^{n/2} \quad (3)$$

Miller and Singh (1994) deduced that the angle derivative (TDR) was defined as the ratio of the first vertical derivative and the horizontal gradient of the potential field. They described the tilt derivative (TDR) equation as the following:

$$\text{TDR} = \tan^{-1}\left(\frac{VDR}{HGM}\right) \quad (4)$$

where VDR represents the vertical derivative of the magnetic field, while HGM is its horizontal gradient magnitude.

The steps of the methodology employed in this study are delineated in the flowchart depicted in Fig. 3.

4 Results and discussion

4.1 Hydrothermal alteration mapping

The following ASTER processing techniques were applied for mapping and detecting the different types of HAM.

4.1.1 Band ratio technique (BR)

The Band Ratio technique (BR) is a robust strategy that involves the division of one spectral band by another, aimed at accentuating characteristics that might remain indiscernible in raw bands (Pour and Hashim 2015; Hegab 2021; El-Qassas et al. 2023). Leveraging spectral reflectance and absorption properties (Fig. 2a), we applied specific band ratios to effectively detect various alteration minerals associated with hydrothermal processes. Specifically, the 4/5 ratio was employed to discern argillic alteration minerals (Fig. 4a), the 4/6 ratio to identify phyllic alteration minerals (Fig. 4b), and the 4/7 ratio

Content courtesy of Springer Nature, terms of use apply. Rights reserved.

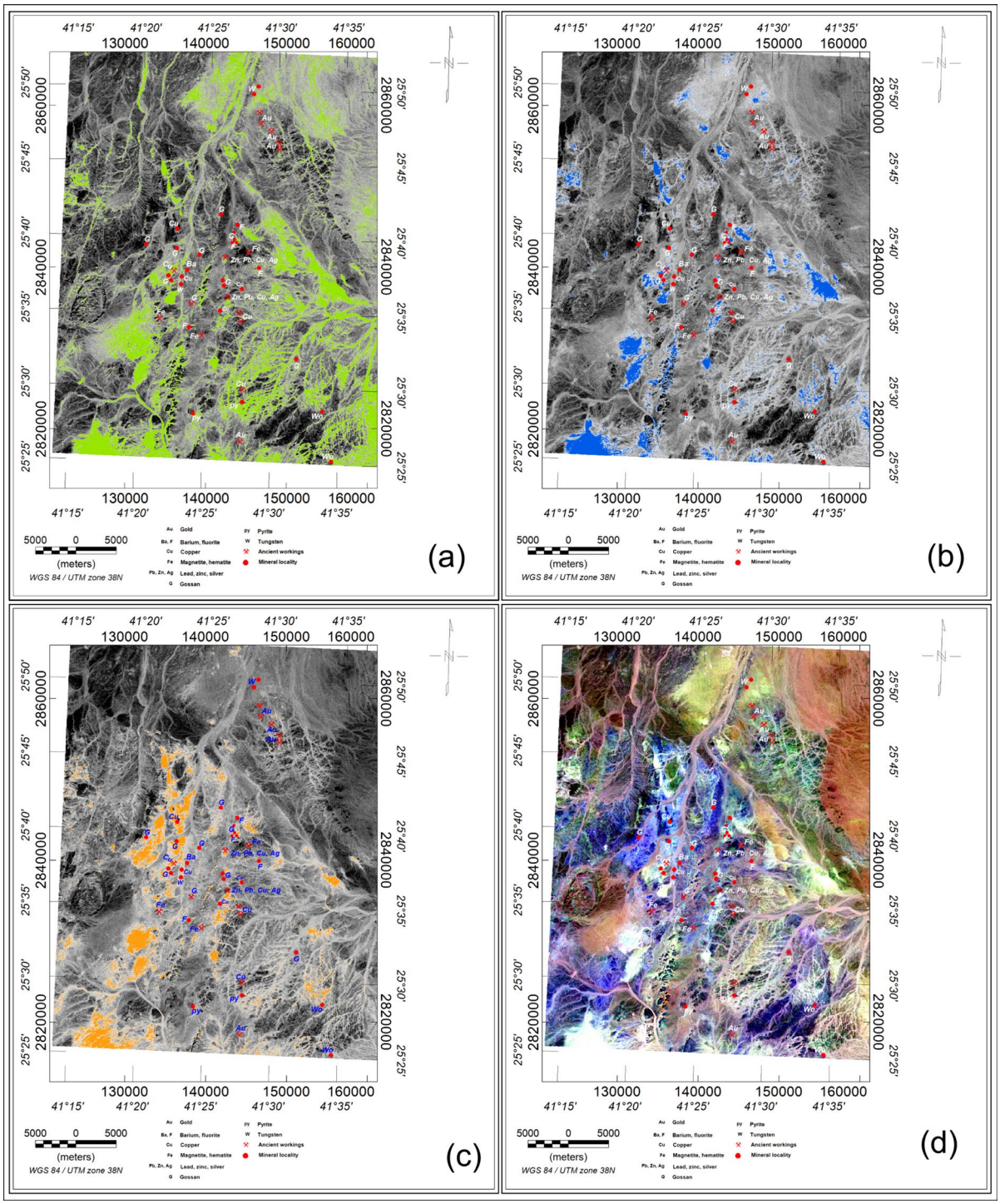

Fig. 4 **a** ASTER band ratio 4/5 image reveals areas where agillic minerals (kaolinite, and allunite) highlighted with green color, **b** ASTER band ratio 4/6 discriminates phyllic minerals (muscovite) highlighted with, **c** ASTER band ratio 4/7 iron minerals (jarosite) are abundant shown in orange tones, and **d** ASTER FCC band ratio (4/5, 4/6. And 4/7) image shows jarosite, argillic, and phyllic alteration minerals in white pixels

Content courtesy of Springer Nature, terms of use apply. Rights reserved.

Table 1 Basic statistics of BR technique, threshold value and confidence degree of endmembers spectra resampled to ASTER

Alteration type	Ratio	Min.	Max.	Mean	SD	Threshold value	Confedence degree (%)
jarosite	B4/B7	0	255	126.4	57.5	241.4	95
Phyllic	B4/B6	0	255	126.7	53.7	234.1	95
Argillic	B4/B5	0	255	142.7	57.3	200	92
Fe-Oxide	B4/B3	0	255	100.2	50.95	253.05	97
Propylitic	B5/B8	0	255	109.97	59.4	228.77	95

to highlight jarosite minerals, which manifested as bright pixels (Fig. 4c). These tailored ratios facilitated the detection of minerals indicative of hydrothermal alteration in rocks. Following the application of Equation No. 1, the threshold for each mineral type was determined, leading to the delineation of their geographical distribution (Table 1, Fig. 4a–c). Additionally, a False Color Composite (FCC) BR (4/5, 4/6, and 4/7) was utilized (Fig. 4d) to discriminate and delineate jarosite, phyllic, and argillic altered rocks, which were represented by light pixels.

Furthermore, we introduced additional ratios in this study, including the (4/3) ratio (Fig. 5a) to identify Fe-oxide/hydroxide phases in altered rocks such as limonite, goethite, and hematite, and the (5/8) ratio for detecting rocks altered by propylitic alteration, which encompass chlorite, epidote, carbonate, and calcite (Fig. 5b). To enhance discrimination among various alteration minerals, we applied the FCC BR transformation image (4/3, 5/8, and 4/7), visualized in RGB format (Fig. 5c). This composite facilitated the differentiation of three primary alteration minerals: (1) a red halo indicating the presence of jarosite minerals, (2) green halos highlighting the distribution of alteration minerals such as chlorite, calcite, and epidote (propylitic alteration minerals), and (3) a blue zone indicating the presence of jarosite minerals.

4.1.2 Principal component analysis (PCA)

PCA stands as an effective tool for accentuating spectral responses linked to specific minerals resulting from hydrothermal alteration within multivariate datasets, such as multispectral satellite images (Crosta et al. 2003; Eldosouky et al. 2021; El-Qassas 2023; Hegab et al. 2023). In our investigation, PCA was employed to analyze both VNIR and SWIR ASTER bands. The eigenvector matrix for the selected ASTER datasets bands is elucidated in Tables 2 and 3.

Table 2 illustrates the eigenvector loadings for the ASTER VNIR and SWIR bands, generated using the computational component of PCA. Notably, reflectance bands crucial for mapping argillic, phyllic, propylitic, and Fe-Oxides alteration minerals exhibit substantial loading in PC8, PC6, PC5, and PC2, respectively, with loadings of 0.707759, −0.621699, −0.620146, and 0.734322, respectively, in bands 5, 4, 8, and 3 (Table 2). Consequently, PC8 and PC2 images manifest argillic and Fe-oxide alteration minerals as bright pixels due to their high positive loading in bands 5 and 3, respectively. Conversely, PC6 and PC5 portray propylitic and phyllic alteration minerals as dark pixels due to their high negative eigenvector loading in bands 8 and 4, necessitating multiplication by −1 to convert dark pixels into bright ones. The threshold for these alteration minerals was established using equation No. 1 (Table 3), with the alteration zones of these minerals depicted as green, orange, violet, and red overlays on density slices (Fig. 6a–d).

4.1.3 Integration of HAM to identify prospective mineralization zones

The mineral alteration maps generated through the processed remote sensing (RS) data techniques (Figs. 4, 5, 6) were integrated using GIS tools to develop a mineralization potentiality model map

Content courtesy of Springer Nature, terms of use apply. Rights reserved.

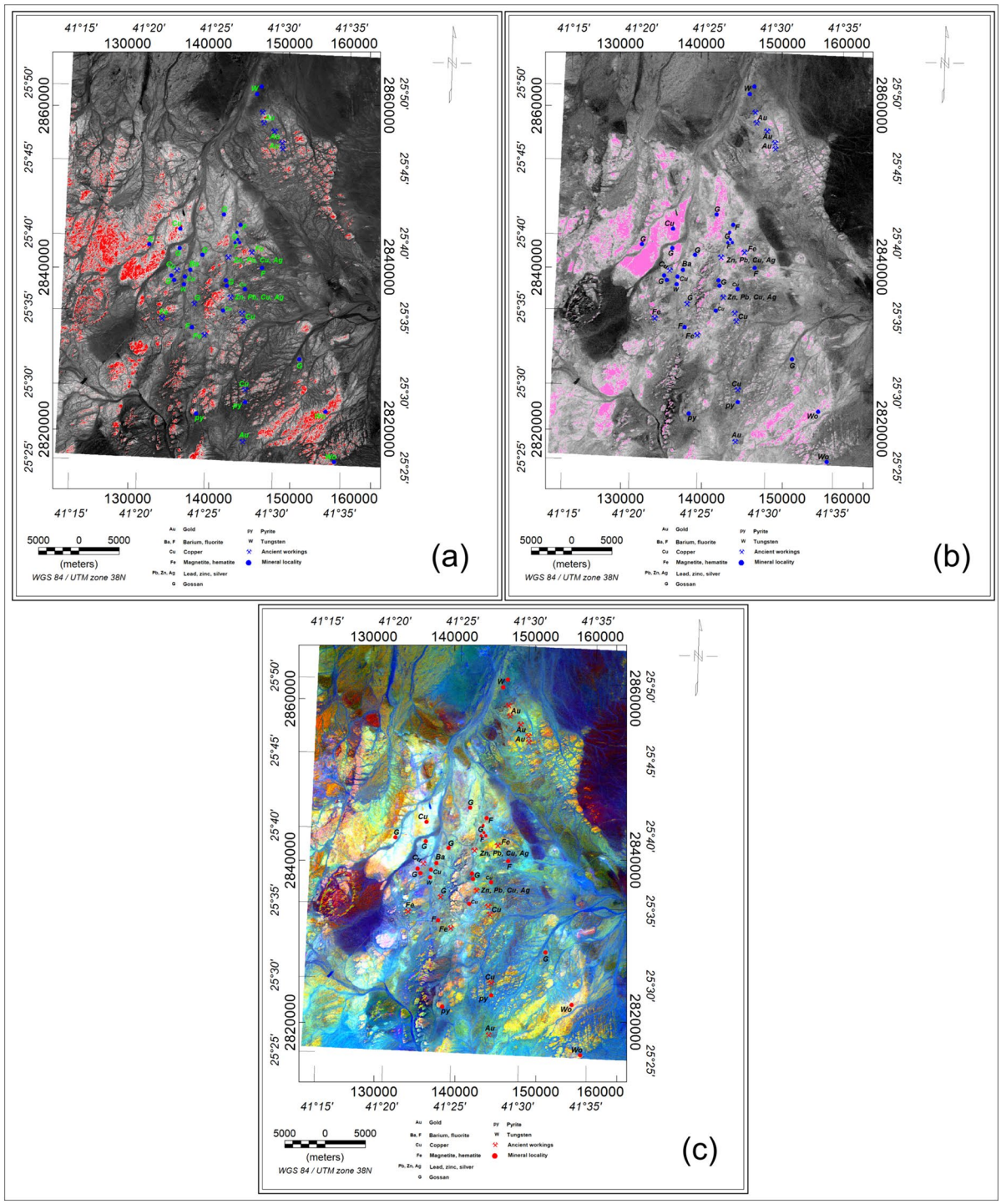

Fig. 5 **a** ASTER band ratio 4/3 image reveals areas where oxide/hydroxide phases as limonite, goethite and hematite altered rocks highlighted with red color, **b** ASTER band ratio 5/8 propylitic alteration minerals as chlorite, epidote, carbonate, and calcite minerals highlighted with magenta color, and **c** ASTER FCC band ratio (4/3, 5/8, and 4/7) image displays in RGB distinguish between several alteration minerals

Content courtesy of Springer Nature, terms of use apply. Rights reserved.

Table 2 Eigenvector matrix for the VNIR + SWIR bands of ASTER datasets

Eigenvectors	B 1	B 2	B3	B4	B5	B6	B7	B 8	B9
PC1	−0.031201	−0.215838	−0.31911	−0.350038	−0.30221	−0.31467	−0.33936	−0.36541	−0.538525
PC2	0.100237	0.525656	0.734322	0.031124	−0.174006	−0.199290	−0.12416	−0.13268	−0.283677
PC3	0.012811	0.106309	0.043190	−0.652152	−0.404704	−0.226947	0.006941	0.328021	0.488461
PC4	−0.011021	0.084498	0.577881	−0.016878	−0.047885	−0.017301	−0.040072	0.036198	0.031631
PC5	0.100281	0.059132	0.084498	−0.179163	0.217046	0.281226	−0.470877	−0.620146	0.474090
PC6	0.032110	0.046863	0.120886	−0.621699	0.368317	0.508414	0.192635	0.115642	−0.389946
PC7	0.016710	0.028187	−0.035430	0.147996	−0.169188	0.375188	−0.719524	0.525342	−0.113832
PC8	0.121104	0.007145	0.010781	−0.102009	0.707759	−0.575433	−0.302019	0.256944	0.012085
PC9	−0.190114	0.291130	0.064310	−0.027531	0.091071	0.209812	−0.413026	−0.023118	−0.050338

Table 3 Basic statistics of PCA technique, threshold value and confidence degree of endmembers spectra resampled to ASTER

Alteration type	PCA	Min	Max	Mean	SD	Threshold value	Confedence degree (%)
Argillic	PC8	0	255	139.95	56.88	253.7	95
Phyllic	PC6	0	255	131.7	56.9	245.5	95
Fe-Oxide	PC2	0	255	121.89	58.31	238.5	95
Propylitic	PC5	0	255	115.22	66.13	247.48	95

(Fig. 7). This comprehensive map was categorized into three distinct probability levels: low, moderate, and high mineralization potential.

The analysis reveals the presence of thirteen intriguing anomalies, denoting high potential mineralization, dispersed across the research zone, each distinguished by a red color (Fig. 7). Anomaly number one is confined to the Maraghan Formation (Fm.) of the Mardamah group north of the Wadi (W) Al Jafen area. Notably, high anomalies 2, 6, 7, 8, and 9 are associated with the Hulayfah group's Nuqrah Fm. Anomalies numbers 3 and 11 are linked to rhyolite, ignimrite, rhyolitic tuff, and breccia, as well as subordinate conglomerate and volcanic sandstone. Anomaly number 3 spans both sides of W. Altarfawy Elsharki, whereas anomaly number 11 is situated northeast of W. Alamariah and southeast of G. El Hamimah, southwest of the study area. Anomalies 4 and 5 are confined to the Afna Fm. of the Hulayfah group, lying between W. Alkhwiash in the east and W. Altarfawy Elgharby in the west. Anomaly number 10 is associated with gabbro and serpentinite rocks around Gabal (G) Dela El Hamimah and W. Altarfawy Elsharki, southwest of the study area. Anomaly number 12 is restricted to older granite, situated at the end of W. Alameirah southwest of the study area, and west of G. Samraa Elseifiah. Finally, anomaly number 13 is associated with Cenozoic deposits behind W. Alameirah and G. Samraa Elseiafiah.

4.2 Aeromagnetic

The Total Magnetic Intensity (TMI) map (Fig. 8a) underwent a reduction-to-the-pole transformation, yielding the RTP map of the Nuqrah area (Fig. 8b). This resultant RTP map reveals varied magnetic anomalies, characterized by both low (negative) and high (positive) magnetic responses. Notably, three discernible magnetic zones (Z1, Z2, and Z3) can be identified. The high magnetic zone (Z1) exhibits a broad range of magnetic values (40 nT to 756.1 nT), serving as the dominant magnetic zone in the study area, evident across the northern, northeastern, western, southern, and eastern sectors (Fig. 8b).

Content courtesy of Springer Nature, terms of use apply. Rights reserved.

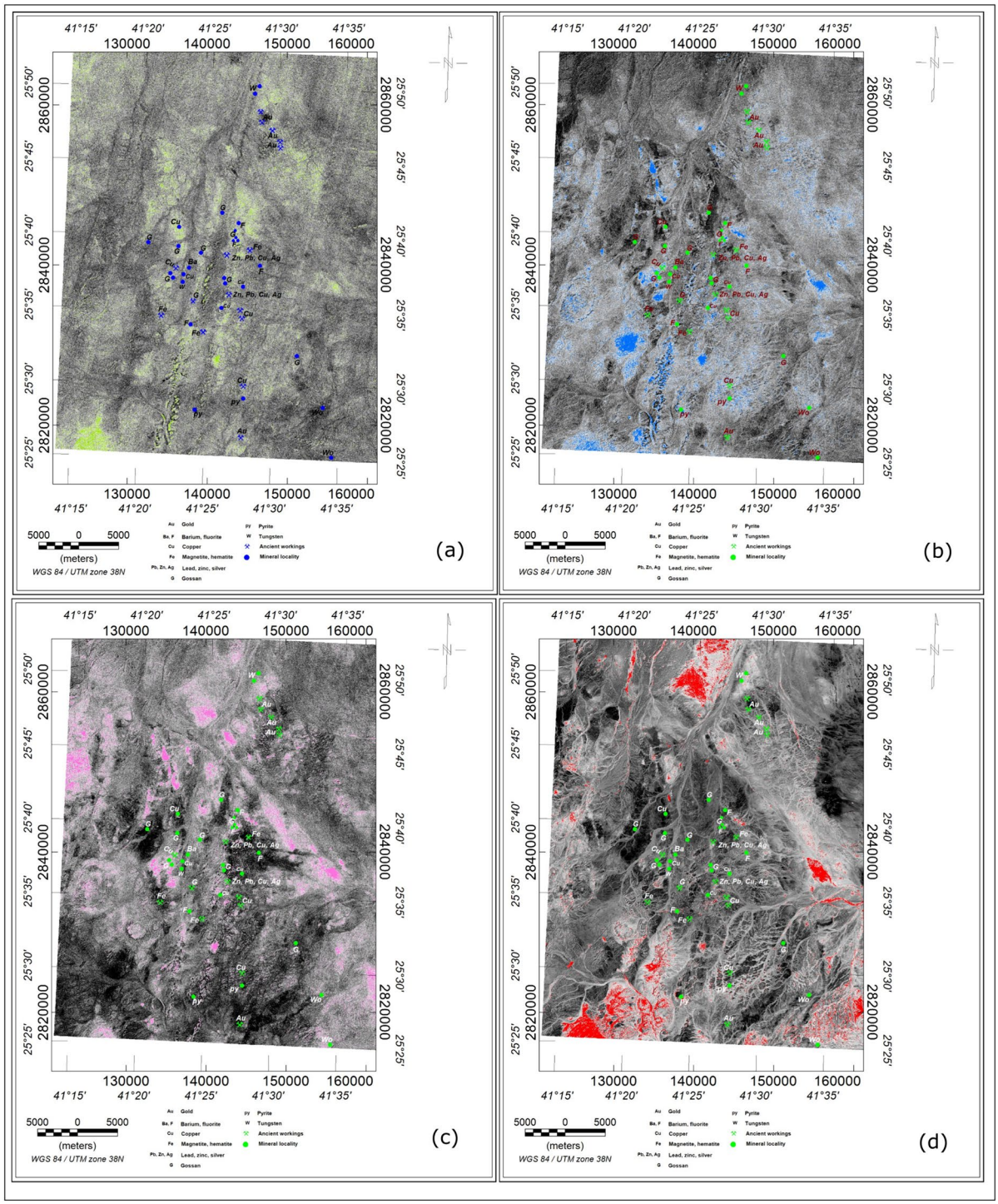

Fig. 6 Showing the resulted PC8 of argillic (**a**), phyllic (**b**), propylitic (**c**), and Fe-Oxides alteration minerals (**d**) images using PCA technique for the input VNIR SWIR bands. Green, orange, violet, red pixels colures represent the alteration type anomalies respectively

Content courtesy of Springer Nature, terms of use apply. Rights reserved.

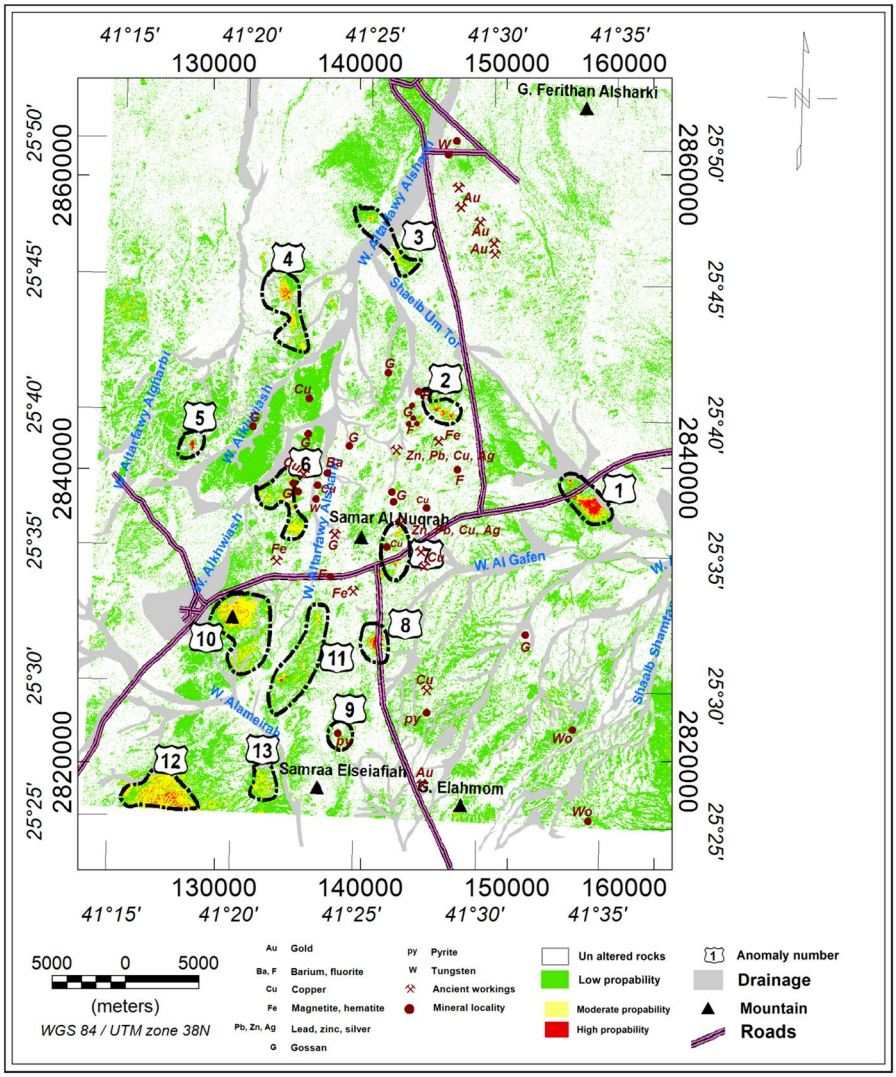

Fig. 7 An integrated alteration mineral predictive model anomaly map of the research region based on ASTER data processing

This zone's magnetic response is likely attributed to surface and subsurface Rharaba complexes (layered gabbro and serpentinite). Meanwhile, the intermediate magnetic zone (Z2) displays values ranging from 40 to −63.3 nT, whereas the low magnetic zone (Z3) encompasses values spanning from −63.3 to −1112.9 nT. These zones correspond predominantly to sedimentary and acidic rocks (Figs. 8b, 1). Furthermore, the frequencies and amplitudes observed in Z3 suggest variations in the depths of the causative magnetic bodies (Fig. 8b).

Utilizing the Power Spectrum approach, we generated residual and regional aeromagnetic maps for the study area, yielding average depths of 434 m and 898 m for residual and regional aeromagnetic maps, respectively (Fig. 9a). The frequency range of the residual component was chosen as 0.46 to 1.54 grid units, which corresponds to shorter wavelengths (Fig. 9b). This highlights the near-surface and small-scale anomalies that are often associated with mineral deposits. The frequency spectrum for the regional component was selected as 0.00 to 0.46

Content courtesy of Springer Nature, terms of use apply. Rights reserved.

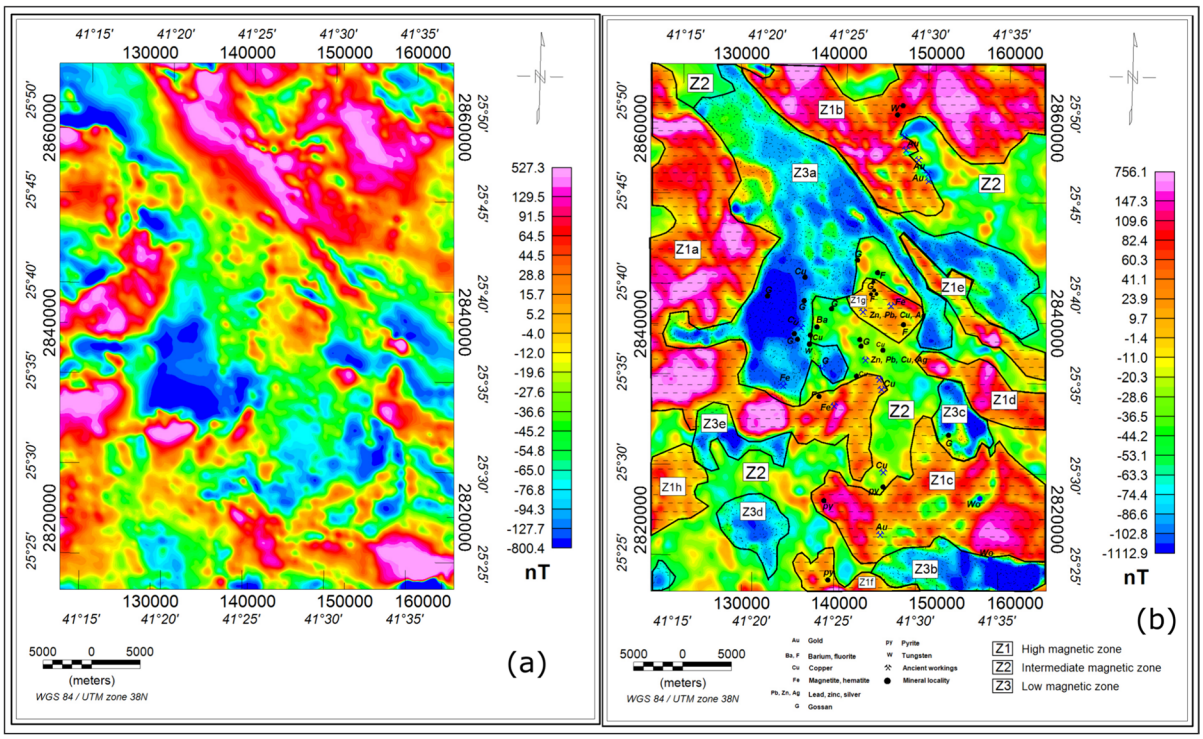

Fig. 8 **a** Total magnetic, and **b** reduced to the pole (RTP) aeromagnetic maps of Nuqrah area, Kingdom of Saudi Arabia (Aero Service 1966)

grid unit. This range corresponds to longer wavelengths, catching the more general, deeper geologic structures that extend over considerable dimensions (Fig. 9c).

The residual aeromagnetic map delineates varying frequencies and amplitudes of low and high magnetic responses across the southeastern corner of the study area, following distinct directional patterns such as NW–SE, NE–SW, E–W, and N–S (Fig. 9b). Additionally, the regional aeromagnetic map (Fig. 9c) reveals a positive magnetic zone (10–109.7 nT) occupying the northern and western sectors, subdivided into two subzones by a NW major fault. These subzones are characterized by relatively high amplitude and frequency, suggesting a shallow magnetic source (Fig. 9c). Conversely, three low magnetic zones are observed in the study region, with the first zone extending from the center to the east, separated into two subzones with distinct amplitudes and frequencies, influenced by the same NW major fault. This feature indicates the influence of the synclinal fold affecting the central, northern, and western regions (Fig. 9c). This observation correlates with the structural sketch map provided in the geological map of the Nuqrah Quadrangle, 25E, Kingdom of Saudi Arabia, compiled by Delfour (1977), wherein the syncline, known as the Simaiyah, and its NW axis consist of the Umm al-Aisah Formation (ju), representing a younger age. Furthermore, examination of the geological and aeromagnetic maps (Figs. 1, 8b, 9c) suggests that the majority of mineralization sites, as indicated on the geological map of the area, align with the synclinal fold geologically associated with the Hulayfah group (Nuqrah Formation and Afna Formation).

Content courtesy of Springer Nature, terms of use apply. Rights reserved.

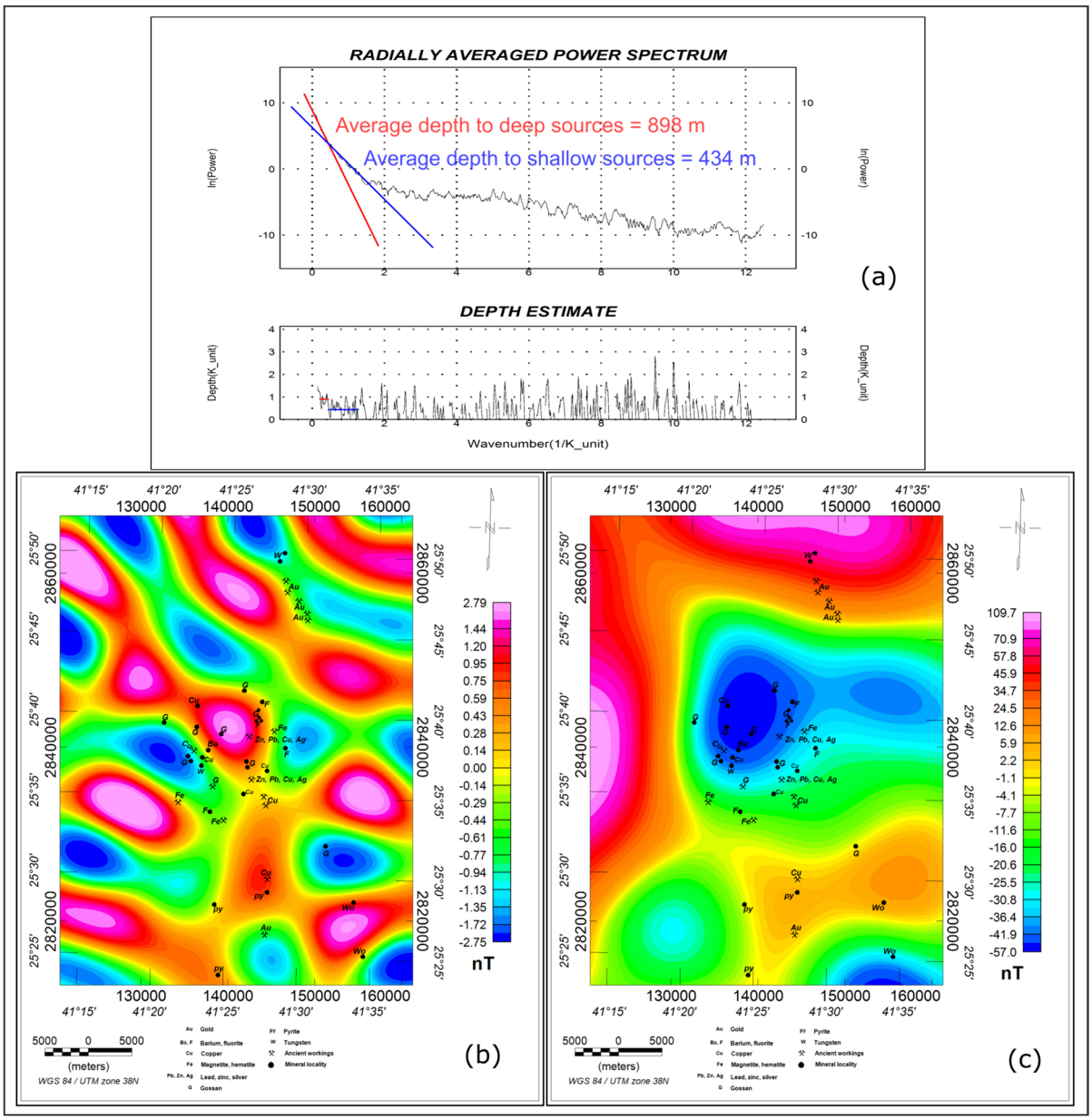

Fig. 9 **a** Radially averaged power spectrum and depth estimate from RTP aeromagnetic map, **b** high-pass (residual), and **c** low-pass (regional) aeromagnetic maps of Nuqrah area, Kingdom of Saudi Arabia

Moreover, we utilized the FVD approach to identify shallow and near-surface lineaments in the RTP data (Fig. 10a). Meanwhile, TDR analysis was employed to ascertain geological features potentially related to shallow structures (Fig. 10b). The zero-contour line depicted the position of vertical contact between positive and negative magnetic anomalies. This clarifies the structural influences within the study area and their control over rock formations.

Content courtesy of Springer Nature, terms of use apply. Rights reserved.

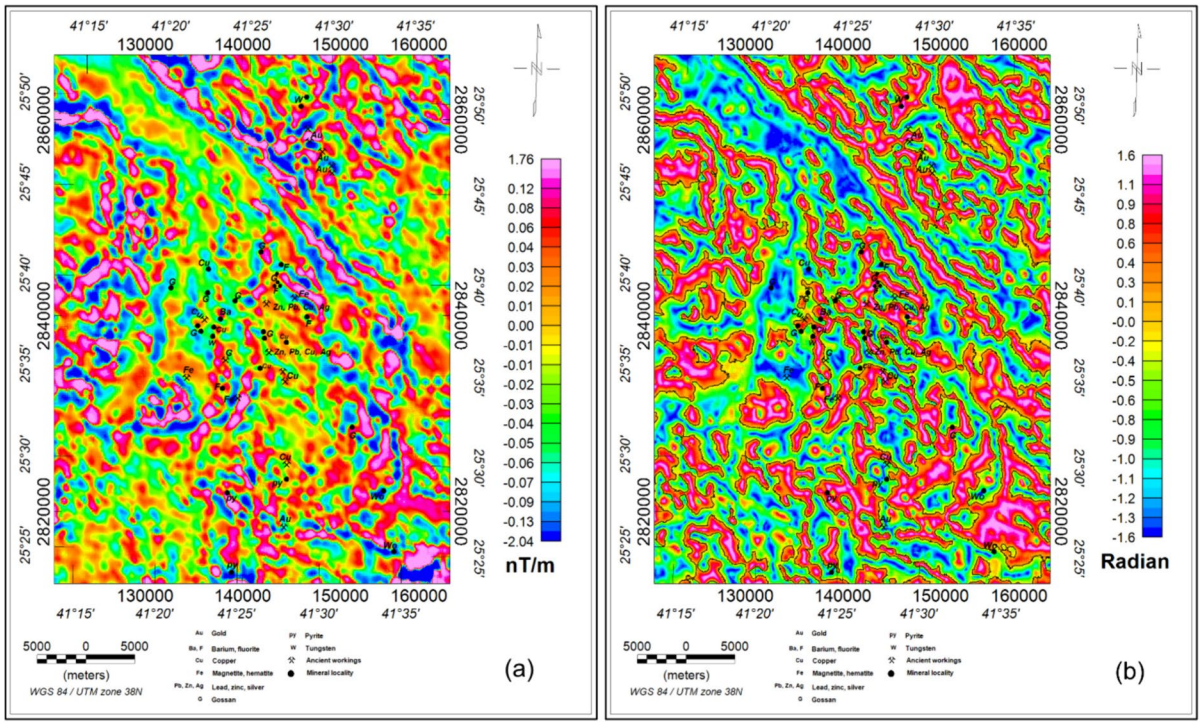

Fig. 10 **a** First vertical derivative (FVD), and **b** tilt derivative (TDR) aeromagnetic maps (continuous black line refer to zero contour values of TDR), Nuqrah area, Kingdom of Saudi Arabia

Additionally, remote sensing and aeromagnetic maps were employed to illustrate the structural lineaments within the study region (Fig. 11a–d). Rose diagrams were constructed to delineate the main structural trends in the research area (Fig. 11a–d). The remote sensing-derived lineament map and rose diagrams (Fig. 11a) identified six major faulting trends, including NE–SW, N–S, ENE–WSW, NNE–SSW, NW–SE, and E–W (in descending order), with WNW–ESE representing a minor faulting trend.

The rose diagram of the RTP aeromagnetic map (Fig. 11b) illustrates that the study region is primarily influenced by the NW–SE, ENE–WSW, E–W, and N–S trends, arranged in decreasing order of magnitude, with shallow and deep structures impacting the Nuqrah area. Near-surface structures affecting the area exhibit trends such as WNW–ESE, NNW–SSE, NW–SE, ENE–WSW, and N–S, ordered in decreasing magnitude in the rose diagram of the residual magnetic map (Fig. 11c). The E–W, N–S, and NE–SW trends are depicted as the deepest trends in the Nuqrah area, grouped in descending order of magnitude on the rose diagram of the regional magnetic map (Fig. 11d).

While previous investigations have explored the mineralization of Saudi Arabia, with few focusing on the Nuqrah area (e.g., Delfour 1975; Collenette and Grainger 1994; Eldosouky et al. 2022c), our paper introduces the first detailed study of the Nuqrah area. The integration of ASTER and aeromagnetic data in this study has facilitated the generation of a mineral potentiality map highlighting promising mineralized sites, validated by known mineral deposits within the Nuqrah area.

Content courtesy of Springer Nature, terms of use apply. Rights reserved.

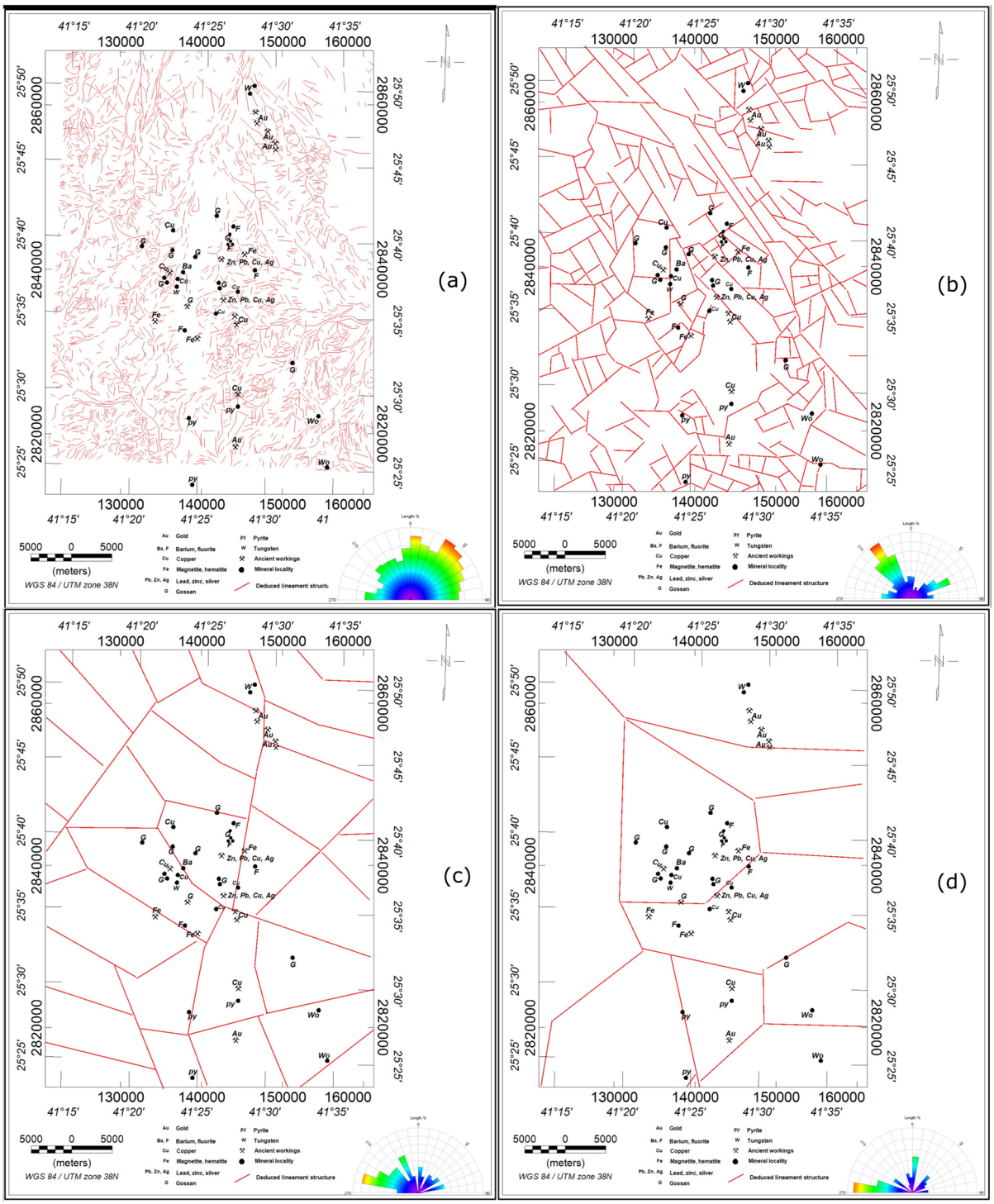

Fig. 11 The lineament structures as deduced from (**a**) remote sensing data, **b** RTP, **c** high-pass, and **d** low-pass aeromagnetic maps and rose diagram (inset), Nuqrah area, Kingdom of Saudi Arabia

Content courtesy of Springer Nature, terms of use apply. Rights reserved.

5 Conclusion

In our research, our main objective was to generate new mineral potentiality maps for the Nuqrah area in Saudi Arabia by integrating ASTER and aeromagnetic (geophysical) data, with the aim of identifying potential targets for mineral exploitation. To achieve our goal, a multifaceted approach employing various techniques was utilized.

Utilizing ASTER satellite data, we used advanced methods including False Colour Composites (FCC), Band Ratios (BR), and Principal Component Analysis (PCA) to delineate the various associated hydrothermal alteration minerals (HAM) within the Nuqrah region. These approaches facilitated the identification and mapping of alteration sites critical for mineral exploration and resource assessment.

Moreover, the reduction-to-the-pole (RTP) map obtained from aeromagnetic data played a pivotal role in delineating magnetic source bodies, providing insights into the geological structures underlying potential mineral deposits. Employing Fast Fourier Transformation (FFT), we generated radially averaged power spectrum, residual, and regional magnetic component maps, enhancing our understanding of the magnetic signatures associated with mineralization. Furthermore, we employed the first vertical derivative (FVD) and tilt derivative (TDR) techniques on the RTP airborne magnetic data to uncover potential mineral-related geologic structures, providing valuable information for targeting mineral exploration efforts.

Our detailed analysis was further enriched by leveraging ASTER data to map alteration sites, enabling us to identify regions exhibiting hydrothermal alteration indicative of mineralization potential. Through remote sensing analysis, we delineated six major faulting trends in the Nuqrah area, including NE–SW, WNW–ESE, N–S, ENE–WSW, NNE–SSW, NW–SE, and E–W trends. Additionally, rose diagrams constructed from aeromagnetic data revealed that the study region is predominantly influenced by NW–SE, ENE–WSW, E–W, and N–S trends, providing important insights into the structural controls governing mineralization in the area.

In conclusion, our study represents a significant contribution in mineral exploration efforts in the Nuqrah region, offering new insights into the geological and structural characteristics underlying mineralization. By integrating ASTER and aeromagnetic data and utilizing advanced analytical techniques, we have produced comprehensive maps that introduce as invaluable tools for detecting prospective mineral targets, thereby laying the groundwork for future resources assessment and exploitation endeavors in the area.

Acknowledgements This research was supported by Researchers Supporting Project number (RSP2024R496), King Saud University, Riyadh, Saudi Arabia.

Authors' contributions Conceptualization, S.S.A., A.M.E., R.A.Y.E. and A.M.A.; methodology, A.M.E., S.S.A., R.A.Y.E., A.E.A.O., and A.M.A.; software, S.S.A., R.A.Y.E., A.E.A.O. and A.M.E.; validation, A.M.E., S.S.A., and A.M.A.; formal analysis, S.S.A., R.A.Y.E., A.E.A.O., A.M.A. and A.M.E.; investigation, A.M.E., S.S.A., R.A.Y.E., A.E.A.O., A.M.A., and P.A.; resources, S.S.A. and A.M.A.; data curation, S.S.A., R.A.Y.E., A.E.A.O., A.M.A. and A.M.E.; writing—original draft preparation, S.S.A., R.A.Y.E., A.E.A.O., A.M.A., P.A. and A.M.E.; writing—review and editing, A.M.E., S.S.A., R.A.Y.E., A.E.A.O., A.M.A., and P.A.; visualization, S.S.A., R.A.Y.E., A.E.A.O., A.M.A., P.A. and A.M.E.; supervision, A.M.E.; project administration, S.S.A.; funding acquisition, S.S.A. All authors reviewed the manuscript. All authors have read and agreed to the published version of the manuscript.

Funding This research was supported by Researchers Supporting Project number (RSP2024R496), King Saud University, Riyadh, Saudi Arabia.

Availability of data and materials No datasets were generated or analysed during the current study.

Declarations

Competing interests The authors declare no competing interests.

Open Access This article is licensed under a Creative Commons Attribution-NonCommercial-NoDerivatives 4.0 International License, which permits any non-commercial use, sharing, distribution and reproduction in any medium or format, as long as you give appropriate credit to the original author(s) and the source, provide a link to the Creative Commons licence, and indicate if you modified the licensed material. You do not have permission under this licence to share adapted material derived from this article or parts of it. The images or other third party material in this article are included in the article's Creative Commons licence, unless indicated otherwise in a credit line to the material. If material is not included in the article's Creative Commons licence and your intended use is not permitted by statutory regulation or exceeds the permitted use, you will need to obtain permission directly from the copyright holder. To view a copy of this licence, visit http://creativecommons.org/licenses/by-nc-nd/4.0/.

Content courtesy of Springer Nature, terms of use apply. Rights reserved.

References

Abdelrahman K, El-Qassas RAY, Fnais MS, Andráš P, Eldosouky AM (2023) Geological structures controlling Au/Ba mineralization from aeromagnetic data: Harrat ad Danun area, Saudi Arabia. Minerals 13:866. https://doi.org/10.3390/min13070866

Abrams MJ, Brown L, Lepley R, Sadowski P (1983) Remote sensing for porphyry copper deposits in Southern Arizona. J Econ Geol 78:591–604

Aero service (1966) Final operational report of airborne magnetic—Arabian geophysical and surveying company

Aita SK, Omar AE (2021) Exploration of uranium and mineral deposits using remote sensing data and GIS applications, Serbal area, Southwestern Sinai, Egypt. Arab J Geosci. https://doi.org/10.1007/s12517-021-08568-0

Arnous MO, Omar AE (2018) Hydro meteorological hazards assessment of some basins in Southwestern Sinai area, Egypt. J Coast Conserv 22:721–743. https://doi.org/10.1007/s11852-018-0604-2

Arnous MO, Azzaz SA, Mowafy AE, Kamar MS, Abdel Hafeez WM (2018) Using space-borne data and photo-lineament indicators to delineate the probable sites of radioactive mineralization at Wadi Dahab area, Southeastern Sinai, Egypt. Curr Sci Int 7(2):213–232

Assran ASM, El Qassas RAY, Yousef MHM (2019) Detection of prospective areas for mineralization deposits using image analysis technique of aeromagnetic data around Marsa Alam-Idfu Road, Eastern Desert, Egypt. Egypt J Petrol 28(1):61–69. https://doi.org/10.1016/j.ejpe.2018.11.002

Bencharef MH, Eldosouky AM, Zamzam S, Boubaya D (2022) Polymetallic mineralization prospectivity modelling using multi-geospatial data in logistic regression: the Diapiric Zone, Northeastern Algeria. Geocarto Int. https://doi.org/10.1080/10106049.2022.2097481

Calvez J-Y, Alsac C, Delfour J, Kemp J, Pellaton C (1983) Geologic evolution of western, central and eastern parts of the northern Precambrian shield: Saudi Arabian Deputy Ministry for Mineral Resources Open-file Report BRGM-OF-03-17, p 57

Clark RN, Swayze GA, Gallagher A, King TVV, Calvin WM (1993) The U.S. Geological Survey, digital spectral library: version 1: 0.2 to 3.0 microns. U.S. Geological Survey Open File Report, pp 93–592

Collenette P, Grainger DJ (1994) Mineral Resources of Saudi Arabia: Saudi Arabian Directorate General of Mineral Resources Special Publication SP-2, p 322

Crosta AP, Souza Filho CR, Azevedo F, Brodie C (2003) Targeting key alteration minerals in epithermal deposits in Patagonia, Argentina, Using ASTER imagery and principal component analysis. Int J Remote Sens. 24:4233–4240

Delfour J (1975) Geology and mineral exploration of the Nuqrah quadrangle (25/41A): Bureau de Recherches Géologiques et Minières Saudi Arabian Mission Technical Record 75-JED-28, p 96, scale 1:100,000

Delfour J (1977) Geologic map of the Nuqrah quadrangle, sheet 25 F, Kingdom of Saudi Arabia: Saudi Arabian Directorate General of Mineral Resources Geologic Map GM 28, scale 1:250,000, p 32

Duyverman HJ, Harris NBW, Hawkesworth CJ (1982) Crustal accretion in the Pan African: Nd and Sr isotope evidence from the Arabian shield. Earth Planet Sci Lett 59:315–326

Ekwok SE, Eldosouky AM, Essa KS, George AM, Abdelrahman K, Fnais MS, Andráš P, Akaerue EI, Akpan AE (2023) Particle swarm optimization (PSO) of high-quality magnetic data of the Obudu basement complex, Nigeria. Minerals 13(9):1209. https://doi.org/10.3390/min13091209

Ekwok SE, George AM, Omori AA, Abdelrahman K, Ugar SI, Andráš P, Morphy MI, Akpan AE, Eldosouky AM (2024) Unveiling the mineral resources and structural patterns in the Middle Benue Trough: a comprehensive exploration using airborne magnetic and radiometric data. Geocarto Int 39:1–23. https://doi.org/10.1080/10106049.2024.2339290

Eldosouky AM, El-Qassas RAY, Pour AB, Mohamed H (2021) Integration of ASTER satellite imagery and 3D inversion of aeromagnetic data for deep mineral exploration. Adv Space Res 68(9):3641–3662. https://doi.org/10.1016/j.asr.2021.07.016

Eldosouky AM, Elkhateeb SO, Mahdy AM, Saad AA, Fnais MS, Abdelrahman K, Andráš P (2022a) Structural analysis and basement topography of Gabal Shilman area, South Eastern Desert of Egypt, using aeromagnetic data. J King Saud Univ Sci 34(2):101764. https://doi.org/10.1016/j.jksus.2021.101764

Eldosouky AM, Pham LT, Henaish H (2022b) High precision structural mapping using edge filters of potential field and remote sensing data: a case study from Wadi Umm Ghalqa area, South Eastern Desert, Egypt. Egypt J Remote Sens Space Sci 25(2):501–513. https://doi.org/10.1016/j.ejrs.2022.03.001

Eldosouky AM, El-Qassas RAY, Pham LT, Abdelrahman K, Alhumimidi MS, El Bahrawy A, Mickus K, Sehsah H (2022c) Mapping main structures and related mineralization of the Arabian shield (Saudi Arabia) using sharp edge detector of transformed gravity data. Minerals 12(71):3

Elkhateeb SO, Eldosouky AM, Khalifa MO, Aboalhassan M (2021) Probability of mineral occurrence in the Southeast of Aswan area, Egypt, from the analysis of aeromagnetic data. Arab J Geosci 14:1514. https://doi.org/10.1007/s12517-021-07997-1

El-Qassas RAY, Ahmed SB, Abd-ElSalam HF, Abu Donia AM (2021) Integrating of remote sensing and airborne magnetic data to outline the geologic structural lineaments that controlled mineralization deposits for the area around Gabal El-Niteishat, Central Eastern Desert, Egypt. Geomaterials 11:1–21. https://doi.org/10.4236/gm.2021.111001

El-Qassas RAY, Abu-Donia AM, Omar AE (2023) Delineation of hydrothermal alteration zones associated with mineral deposits, using remote sensing and airborne geophysics data. A case study: El-Bakriya area, Central Eastern Desert, Egypt. Acta Geod Geophys 58:71–107. https://doi.org/10.1007/s40328-023-00405-y

Gunn PJ (1975) Linear transformation of gravity and magnetic fields. Geophys Prospect 23(2):300–312. https://doi.org/10.1111/j.1365-2478.1975.tb01530.x

Hajibapir G, Lotfi M, Zarifi AZ, Nezafati N (2014) Application of different image processing techniques on Aster and

Content courtesy of Springer Nature, terms of use apply. Rights reserved.

ETM+ images for exploration of hydrothermal alteration associated with copper mineralizations mapping Kehdolan Area (Eastern Azarbaijan Province-Iran). Open J Geol 4(11):15. https://doi.org/10.4236/ojg.2014.411043

Heck G (1999) Gold mining in Arabia and the rise of the Islamic state. J Econ Soc History Orient 42(3):364–395

Hegab MA (2021) Remote sensing and gamma-ray spectrometry based gold related alteration zones detection: case study (Um Balad area), North Eastern Desert, Egypt. Pure Appl Geophys 178:3909–3931. https://doi.org/10.1007/s00024-021-02865-1

Hegab MA, Mousa SE, Salem SM, Farag K, GabAllah H (2022) Gold-related alteration zones detection at the Um Balad Area, Egyptian Eastern Desert, using remote sensing, geophysical, and GIS data analysis. J Afr Earth Sci. https://doi.org/10.1016/j.jafrearsci.2022.104715

Hegab MA, Mousa SE, Salem SM, Moustafa MS (2023) ASTER and aerospectrometric data analysis for gold exploration: case study at Um Balad Area, North Eastern Desert, Egypt. In: Gad AA, Elfiky D, Negm A, Elbeih S (eds) Applications of remote sensing and GIS based on an innovative vision. ICRSSSA 2022. Springer Proceedings in Earth and Environmental Sciences. Springer, Cham. https://doi.org/10.1007/978-3-031-40447-4_6

Hunt GR (1977) Spectral signatures of particulate minerals in the visible and near infrared. Geophysics 42:501–513

Johnson PR, Andresen A, Collins AS, Fowler AR, Fritz H, Ghebreab W, Stern RJ et al (2011) Late Cryogenian–Ediacaran history of the Arabian–Nubian shield: a review of depositional, plutonic, structural, and tectonic events in the closing stages of the northern East African Orogen. J Afr Earth Sci 61(3):167–232

Johnson PR (2005) Proterozoic geology of western Saudi Arabia, northeastern sheet (revised, digital edition): Saudi Geological Survey Open-File Report SGS-OF-2005-2, p 39

Kharbish S, Eldosouky AM, Amer O (2022) Integrating mineralogy, geochemistry and aeromagnetic data for detecting Fe–Ti ore deposits bearing layered mafic intrusion, Akab El-Negum, Eastern Desert, Egypt. Sci Rep 12:15474. https://doi.org/10.1038/s41598-022-19760-x

Kingdom of Saudi Arabia Ministry of Petroleum and Mineral Resources. (1977). Geology of the Nuqrah Quadrangle, 25E, Kingdom of Saudi Arabia. Scale 1:250000

Mahdi AM, Eldosouky AM, El Khateeb SO, Youssef AM, Saad AA (2022) Integration of remote sensing and geophysical data for the extraction of hydrothermal alteration zones and lineaments; Gabal Shilman basement area, Southeastern Desert, Egypt. J Afr Earth Sci 194:104640. https://doi.org/10.1016/j.jafrearsci.2022.104640

Miller HG, Singh V (1994) Potential field tilt: a new concept for location of potential field sources. J Appl Geophys 32(2–3):213–217. https://doi.org/10.1016/0926-9851(94)90022-1

Morony M (2019) The early Islamic mining boom. J Econ Soc Hist Orient 62(1):166–221. https://doi.org/10.1163/15685209-12341477

Omar AE (2021) Application of geospatial approaches to prospect radioactive minerals in the Um Bogma younger granites, Southwestern Sinai, Egypt. Arab J Geosci 14:328. https://doi.org/10.1007/s12517-021-06684-5

Omar AE, Korany AK, Abdel-Halim KA (2021) Calculation of natural external radiation dose rate for environmental impact assessment, case study: Abu Zenima area, Southwestern Sinai, Egypt. Int J Environ Analyt Chem. https://doi.org/10.1080/03067319.2021.1895133

Omar AE, Sakr MAH, Taalab SA, Bakhit AA, Pugliese M, La Verde G, Hanfi MY (2023a) Geotechnical and environmental radioactivity investigations at Al Sādis Min Uktōber city, Cairo municipality (Egypt), for the high-speed railway construction. Appl Radiat Isot. https://doi.org/10.1016/j.apradiso.2023.110664

Omar AE, Abdel-Halim KA, Arnous MO (2023) State of the practice worldwide: utilizing hydrogeochemical data and GIS tools to assess the groundwater quality in arid region: example from Wadi Feiran Basin, Southwestern Sinai, Egypt. Groundw Monit Remidation 2:2. https://doi.org/10.1111/gwmr.12625

Pham LT, Kafadar O, Oksum E, Eldosouky AM (2021) An improved approach for detecting the locations of the maxima in interpreting potential field data. Arab J Geosci 14:43. https://doi.org/10.1007/s12517-020-06399-z

Pour A, Hashim M (2015) Hydrothermal alteration mapping using Landsat 8 data, Sar Cheshmeh copper mining district. SE Iran J Taibah Univ Sci 9(2):155–166. https://doi.org/10.1016/j.jtusci.2014.11.008

Rowan LC, Mars JC (2003) Lithologic mapping in the Mountain Pass, California area using Advanced Spaceborne Thermal Emission and Reflection Radiometer (ASTER) data. Remote Sens Environ 84:350–366

Rowan LC, Hook SJ, Abrams MJ, Mars JC (2003) Mapping hydrothermally altered rocks at Cuprite, Nevada, using the Advanced Spaceborne Thermal Emission and Reflection Radiometer (ASTER), a new satellite-imaging system. Econ Geol 98:1019–1027

Saad AM, Sakr MA, Omar AE, Temsah YA (2020) Assessment of radioactivity and geotechnical characteristics of soil foundation for suitability of safe urban extension using geospatial technology New Sahl Hasheesh Marin Port, Eastern Desert, Egypt. Int J Environ Analyt Chem. https://doi.org/10.1080/03067319.2020.1802444

Tommaso IM, Rubinstein N (2007) Hydrothermal alteration mapping using ASTER data in the Infiernillo porphyry deposit, Argentina. Ore Geol Rev 32:275–290

Publisher's Note Springer Nature remains neutral with regard to jurisdictional claims in published maps and institutional affiliations.

Content courtesy of Springer Nature, terms of use apply. Rights reserved.

Terms and Conditions

Springer Nature journal content, brought to you courtesy of Springer Nature Customer Service Center GmbH (“Springer Nature”).
Springer Nature supports a reasonable amount of sharing of research papers by authors, subscribers and authorised users (“Users”), for small-scale personal, non-commercial use provided that all copyright, trade and service marks and other proprietary notices are maintained. By accessing, sharing, receiving or otherwise using the Springer Nature journal content you agree to these terms of use (“Terms”). For these purposes, Springer Nature considers academic use (by researchers and students) to be non-commercial.
These Terms are supplementary and will apply in addition to any applicable website terms and conditions, a relevant site licence or a personal subscription. These Terms will prevail over any conflict or ambiguity with regards to the relevant terms, a site licence or a personal subscription (to the extent of the conflict or ambiguity only). For Creative Commons-licensed articles, the terms of the Creative Commons license used will apply.
We collect and use personal data to provide access to the Springer Nature journal content. We may also use these personal data internally within ResearchGate and Springer Nature and as agreed share it, in an anonymised way, for purposes of tracking, analysis and reporting. We will not otherwise disclose your personal data outside the ResearchGate or the Springer Nature group of companies unless we have your permission as detailed in the Privacy Policy.
While Users may use the Springer Nature journal content for small scale, personal non-commercial use, it is important to note that Users may not:

1. use such content for the purpose of providing other users with access on a regular or large scale basis or as a means to circumvent access control;
2. use such content where to do so would be considered a criminal or statutory offence in any jurisdiction, or gives rise to civil liability, or is otherwise unlawful;
3. falsely or misleadingly imply or suggest endorsement, approval , sponsorship, or association unless explicitly agreed to by Springer Nature in writing;
4. use bots or other automated methods to access the content or redirect messages
5. override any security feature or exclusionary protocol; or
6. share the content in order to create substitute for Springer Nature products or services or a systematic database of Springer Nature journal content.

In line with the restriction against commercial use, Springer Nature does not permit the creation of a product or service that creates revenue, royalties, rent or income from our content or its inclusion as part of a paid for service or for other commercial gain. Springer Nature journal content cannot be used for inter-library loans and librarians may not upload Springer Nature journal content on a large scale into their, or any other, institutional repository.
These terms of use are reviewed regularly and may be amended at any time. Springer Nature is not obligated to publish any information or content on this website and may remove it or features or functionality at our sole discretion, at any time with or without notice. Springer Nature may revoke this licence to you at any time and remove access to any copies of the Springer Nature journal content which have been saved.
To the fullest extent permitted by law, Springer Nature makes no warranties, representations or guarantees to Users, either express or implied with respect to the Springer nature journal content and all parties disclaim and waive any implied warranties or warranties imposed by law, including merchantability or fitness for any particular purpose.
Please note that these rights do not automatically extend to content, data or other material published by Springer Nature that may be licensed from third parties.
If you would like to use or distribute our Springer Nature journal content to a wider audience or on a regular basis or in any other manner not expressly permitted by these Terms, please contact Springer Nature at

onlineservice@springernature.com